

A numerical investigation of turbulent flows in a spanwise rotating channel

Nan-Sheng Liu, Xi-Yun Lu *

Department of Modern Mechanics, University of Science and Technology of China, Hefei, Anhui 230026, PR China

Received 22 April 2005; received in revised form 12 October 2005; accepted 19 November 2005

Available online 28 February 2006

Abstract

A numerical investigation of fully developed turbulent flow in a spanwise rotating channel is performed to study turbulence characteristics subject to system rotation. The work provides insight into several salient features of the spanwise rotating turbulent channel flows, including the near-wall vortical structures, turbulence energy cascade and redistribution, and vortex stretching. The influence of system rotation on the near-wall vortical structures is investigated based on the vorticity fluctuations and their probability density functions (PDF). The properties of the Lamb vector fluctuation and the corresponding PDF are examined to reveal the effect of rotation on the turbulence energy cascade and production in the rotating channel. The budgets of Reynolds stresses and fluctuating enstrophy are analyzed to elucidate the role of the Coriolis force on turbulence energy redistribution between the streamwise and wall-normal directions and the mechanisms of vortex stretching for the generation of the vorticity fluctuations near the pressure and suction walls.
© 2006 Elsevier Ltd. All rights reserved.

1. Introduction

Rotating turbulent flow exists widely in various industrial, geophysical and astrophysical applications. In these flows, the rotation induces additional body forces, i.e., centrifugal and Coriolis forces, acting on the turbulent flow, so that the momentum transfer mechanism becomes more complicated. Turbulent flow in rotating channel is a typical case due to its simple geometry and becomes a preferred candidate to investigate the influence of system rotation on the turbulence statistics, the near-wall structures, and the dynamic process. Some typical work on the rotating turbulent channel flows has been carried out experimentally and numerically.

The remarkable feature of a spanwise rotating channel flow is the rotational-induced alteration of turbulence level, suppressed near the stabilized (suction) wall and enhanced near the destabilized (pressure) wall [1,2]. The tendency of near-wall turbulence to stabilization or destabilization can be indicated by an equivalent gradient ‘Richardson num-

ber’ Ri_g , which is drawn from an analogy among the influences of rotation, streamline curvature and thermal stratification on turbulent flows [3]. This analogy leads to a criterion that the level of turbulence subject to system rotation is augmented when $Ri_g > 0$ and damped when $Ri_g < 0$. Tritton and Davies [4] and Tritton [5] drew the similar conclusion as a result of ‘displaced particle analysis’ on rotating shear flow. Kristoffersen and Andersson [6] employed this criterion to interpret the turbulence augmentation and suppression in the wall regions of the spanwise rotating channel and revealed the relaminarized behavior near the suction wall. Similar effects of system rotation on the turbulence in a boundary layer were also studied [7–9].

The coherent structures are closely associated with the near-wall turbulence sweep and ejection events. Moin and Kim [10] succeeded in connecting the turbulence behaviors with the near-wall structures in their study of pure shear channel flow and affirmed that the coherent structures are related to the most energetic events, which are responsible for the turbulence production and dissipation in the wall regions. Orlandi [11] attributed the suppression of turbulence in a rotating pipe to the alteration of the strength and size of coherent structures near the wall. However,

* Corresponding author. Tel.: +86 551 3603223; fax: +86 551 3606459.
E-mail address: xlu@ustc.edu.cn (X.-Y. Lu).

little work is carried out to reveal the relation between coherent structures and turbulence characteristics in the near-wall region of the spanwise rotating channel.

The probability density functions (PDF) of turbulence fluctuations are relevant to the motion of small scales in the wall-shear turbulence [12,13]. Orlandi [11] asserted that the PDF of helicity and Lamb vector fluctuations are closely related to the wall drag reduction and turbulence statistics of rotating pipe flow. As the spanwise rotating channel flow is characterized by the rotational-induced alteration of near-wall turbulence level, the vortical structures near the suction and pressure walls are different from those in the axially rotating pipe flow in which the rotation axis is parallel to the mean flow. Thus, one motivation of this study is to reveal how the near-wall vortical structures and statistics react to the existence of the spanwise rotation based on the analysis of the PDFs of turbulence fluctuations.

It is recognized that the Lamb vector fluctuation $\vec{u}' \times \vec{\omega}'$ represents the non-linear interaction exchanging energy between different scales in turbulence [14,15]. The regions with strong $\vec{u}' \times \vec{\omega}'$ are always characterized by the strong turbulent kinetic energy cascade [11]. It is due to the fact that, in the budget of turbulent kinetic energy, $\vec{u}' \times \vec{\omega}'$ appears in the term interpreted as the turbulence energy cascade from large to small scales, which also contributes to turbulence energy production. In the axially rotating pipe flow, less energy production and drag are attributed to the behavior of $\vec{u}' \times \vec{\omega}'$. The Lamb vector fluctuation has received special attention to study turbulence energy cascade [16]. Hence, the other motivation of this study is to elucidate the role of the Coriolis force in the process of turbulence energy cascade and production in the spanwise rotating channel flow by means of the analysis of the Lamb vector fluctuation.

The budgets of Reynolds stresses provide detailed information on the dynamical characteristics of turbulence, such as production, redistribution and dissipation of turbulent kinetic energy, and are of great help in the turbulence closures. Mansour et al. [17] evaluated the budgets of Reynolds stresses and determined the coefficients in their asymptotic expansions of velocity and pressure fluctuations in the wall region based on the DNS database [18]. Durbin [19] employed the budget terms to validate the turbulence model for the prediction of the wall damping of wall-normal turbulent kinetic energy. Orlandi [20] dealt with the turbulence budgets to reveal the modification of near-wall structures in the rotating pipe flow. Note that, in the transport equation for turbulent kinetic energy of rotating turbulence, the Coriolis force term does not occur explicitly, which indicates that the Coriolis force acts as a role to redistribute turbulent kinetic energy among the turbulence fluctuations. To reveal the mechanism of energy redistribution related to the Coriolis force in rotating turbulence, it is also needed to deal with the budgets in the transport equation for Reynolds stresses in detail.

Further, the analysis of the budgets in the transport equation for fluctuating enstrophy ($\langle \omega'_i \omega'_i \rangle / 2$) is also of

great help in understanding the stretching of vorticity fluctuations in the wall region and the generation of near-wall vortical structures [20–24]. Dimitropoulos et al. [25] reported that the turbulent flow with drag reduction is characterized by a significant suppression of vortex stretching–squeezing activity and containing more ordered structures by the decreasing of vortex stretching terms in the fluctuating enstrophy budget. Since the changes of the near-wall vortical structures near the suction and pressure

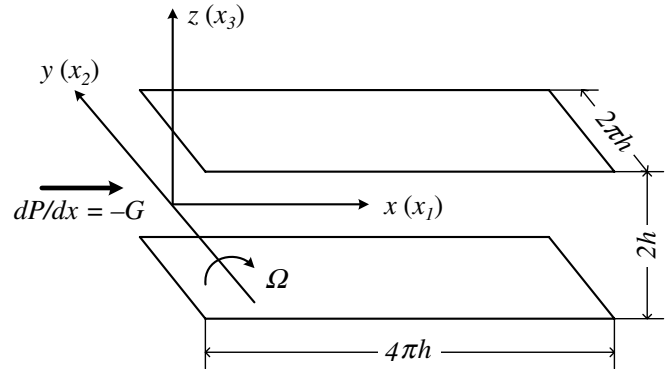


Fig. 1. Sketch of the spanwise rotating turbulent channel flow.

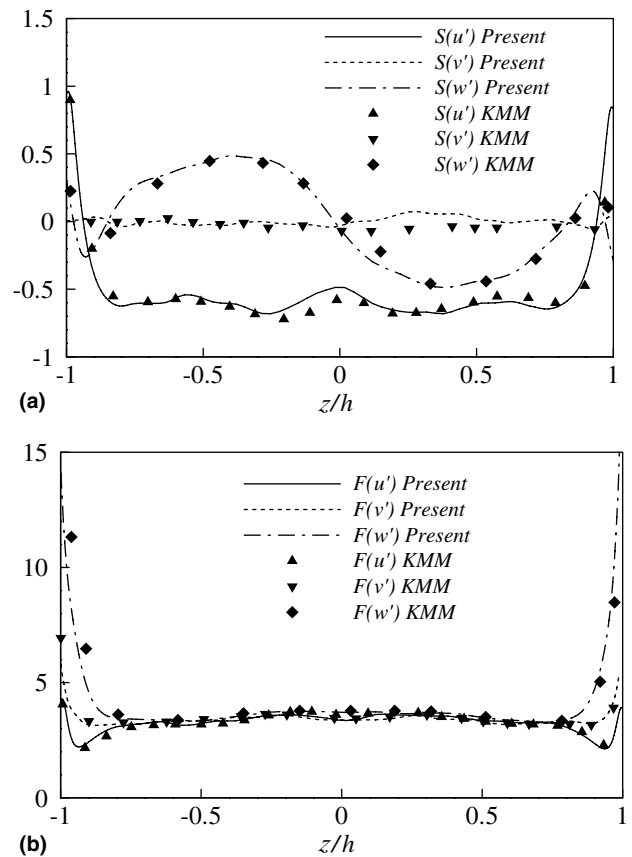


Fig. 2. Skewness and flatness for turbulent channel flow and comparison with previous results: (a) skewness, (b) flatness. Here, “KMM” represents the results in [18] in this and the following figures.

walls occur in the spanwise rotating channel flow, our further motivation is to study the relations of the vortex stretching with the mean flow, velocity fluctuations and back ground rotation.

This paper is organized as follows. The mathematical formulation is described in Section 2. The numerical

method is given in Section 3. In Section 4, some typical characteristics on the spanwise rotating channel flows, e.g., the near-wall vortical structures, turbulence energy cascade, production and redistribution, and vortex stretching, are discussed. Finally, concluding remarks are summarized in Section 5.

2. Mathematical formulation

The incompressible Navier–Stokes equations are used for the direct simulation of fully developed turbulent flow in a spanwise rotating channel. As shown in Fig. 1, to normalize the governing equations, the global friction velocity u_τ is used as the velocity scale, and the half-height of the channel h as the length scale. The non-dimensional governing equations are given as

$$\frac{\partial u_i}{\partial x_i} = 0 \tag{1}$$

$$\frac{\partial u_i}{\partial t} + \frac{\partial (u_i u_j)}{\partial x_j} = -\frac{\partial p}{\partial x_i} + \delta_{li} + \frac{1}{Re_\tau} \frac{\partial^2 u_i}{\partial x_j \partial x_j} - N_\tau \varepsilon_{ijk} \frac{\Omega_j}{\Omega} u_k \tag{2}$$

where p represents the effective pressure combined with the centrifugal force. The parameters are the rotation number and the Reynolds number, which are defined as

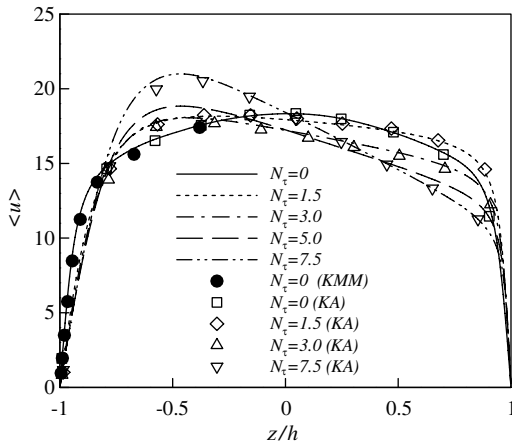


Fig. 3. Mean velocities and comparison with previous results. Here, “KA” represents the results in [6] in this and the following figures.

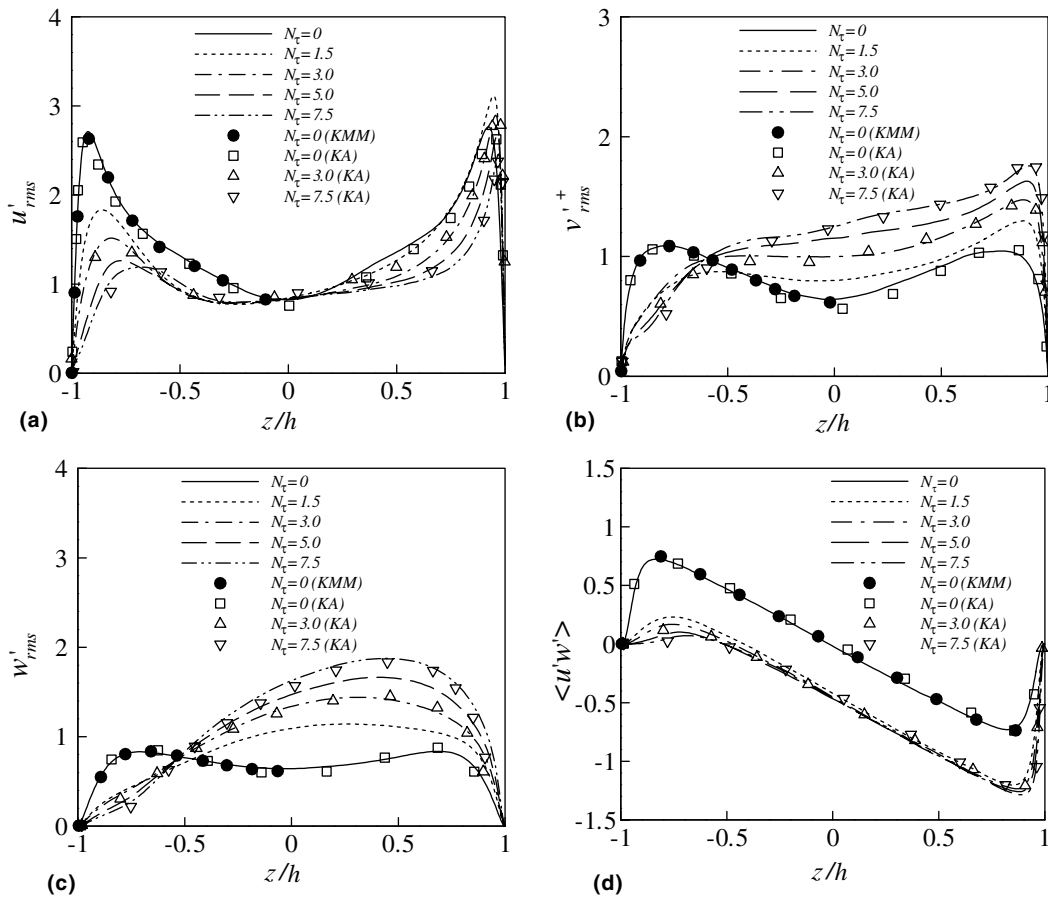


Fig. 4. Turbulence statistics and comparison with previous results: (a) streamwise turbulence intensity, (b) spanwise intensity, (c) wall-normal intensity, (d) shear stress $\langle u'w' \rangle$.

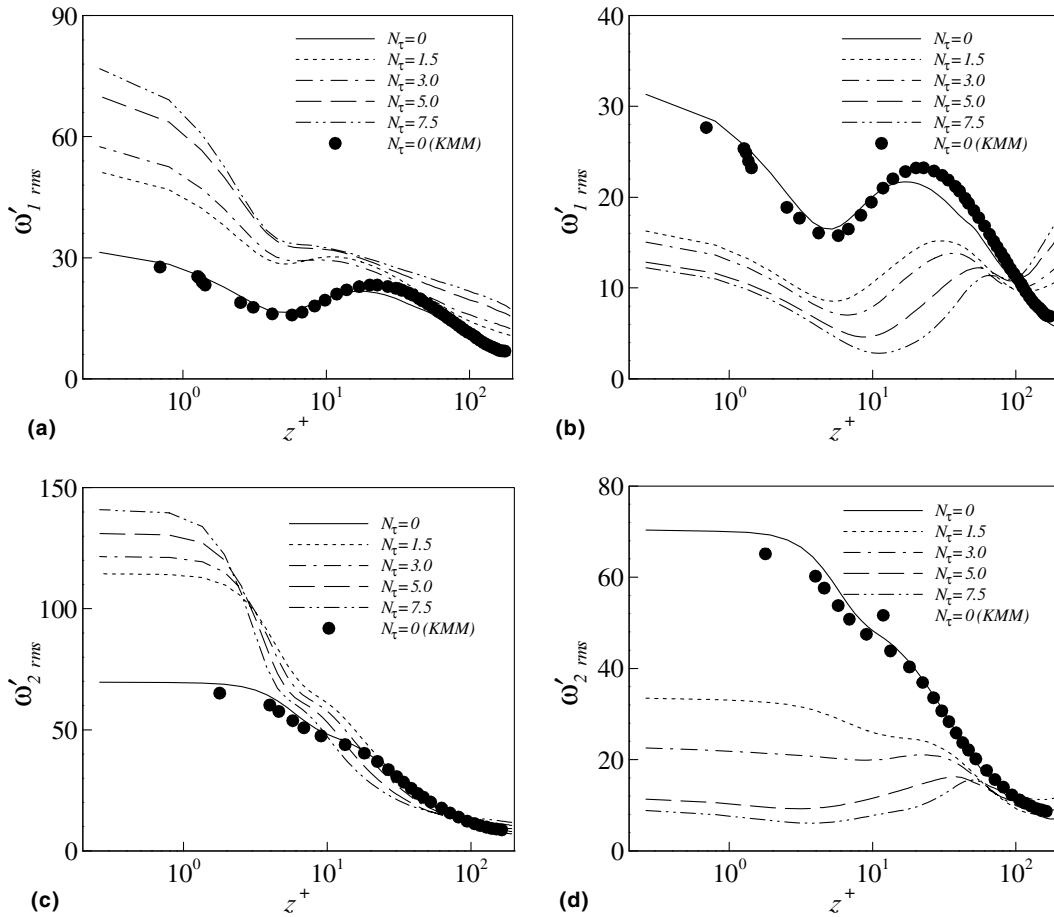


Fig. 5. Profiles of the vorticity fluctuations and comparison with previous results: (a) $\omega'_{1,rms}$ in the pressure side, (b) $\omega'_{1,rms}$ in the suction side, (c) $\omega'_{2,rms}$ in the pressure side, (d) $\omega'_{2,rms}$ in the suction side.

$N_\tau = 2\Omega h/u_\tau$ and $Re_\tau = u_\tau h/\nu$, respectively, with Ω being the angular speed of rotating frame and ν the kinematic viscosity. The global friction velocity u_τ is defined as [6]

$$u_\tau = \left(\left| \frac{h}{\rho} \frac{d\bar{p}}{d\bar{x}} \right| \right)^{1/2} \quad (3)$$

where $d\bar{p}/d\bar{x}$ is the dimensional pressure gradient. No-slip boundary condition is used on the channel walls and periodic boundary conditions are employed in the streamwise and spanwise directions.

3. Numerical method

To solve Eqs. (1) and (2), a fractional-step method was employed. Spatial derivatives are discretized by the second-order central difference. Time advancement is carried out by the semi-implicit scheme combining the Crank–Nicolson scheme for the viscous terms and the three-stage Runge–Kutta scheme for the convection terms. The discretized formulation was described in [26]. This method simplifies the boundary condition of the non-solenoidal velocity field and remains the feature of the algorithm in [27,28].

In this study, the Reynolds number Re_τ is chosen as 194 and the rotation number varies from 0 to 7.5. The grid

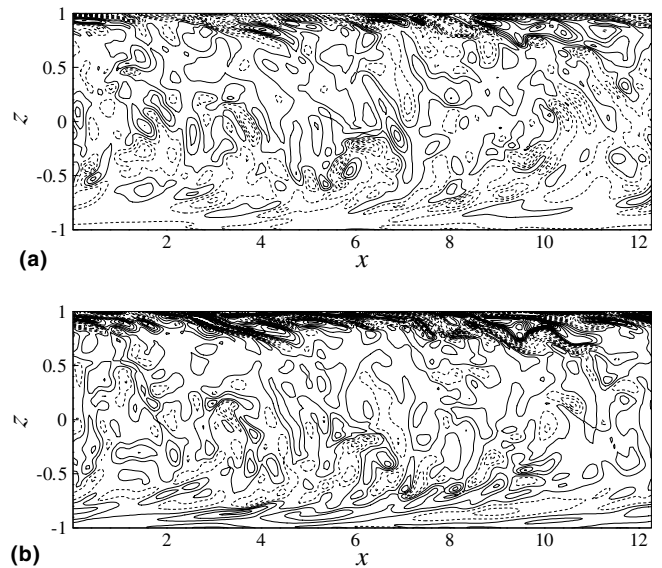


Fig. 6. Contours of the vorticity fluctuations in (x,z) plane at $N_\tau = 3.0$: (a) streamwise component ω'_1 , (b) spanwise component ω'_2 . Here, contour increments $\Delta\omega'_1 = 20$ and $\Delta\omega'_2 = 10$.

number is $193 \times 129 \times 161$ with the corresponding computational domain $4\pi h \times 2\pi h \times 2h$ in the streamwise, spanwise, and wall-normal directions, respectively. A stretching transformation is employed to increase the grid resolution in the wall regions. The grid point closest to the wall is located at $z^+ = 0.3$ approximately, while the largest spacing is about $\Delta z^+ = 4.5$ in the center of the channel, where z^+ is defined as $z^+ = (1 - |z/h|)Re_\tau$. Uniform grids are employed in the streamwise and spanwise directions with the grid spacing $\Delta x^+ = 12.6$ and $\Delta y^+ = 9.5$, respectively. This grid system has been ensured to be capable of resolving all essential scales of the turbulence.

It is worthwhile to mention that the performance and reliability of the numerical method used in this study have been verified extensively [11,20,29]. It was ensured that the second- and higher-order turbulence statistics compared well with available DNS results calculated by spectral methods and with experimental data. The finite difference schemes with the second-order accuracy are widely used in the DNS of turbulent and transitional flows, e.g., rotating channel flow [6,30], annular pipe flow [31], oscillatory flow in the boundary layer and pipe [32,33], and turbulent Rayleigh–Bénard convection flow [34].

To demonstrate that the results calculated by the numerical methods used are reliable, extensive validations have

been undertaken in this study and in our previous work [35–43]. Usually, the high-order statistical turbulence quantities are more sensitive to the numerical methods. Thus, comparisons of the skewness and flatness of the velocity fluctuations for turbulent channel flow are shown in Fig. 2. It is seen that our results are in good agreement with those predicted by the spectral method [18]. Furthermore, some typical comparisons with the previous results, including the mean velocity, turbulence intensities and shear stress, and vorticity fluctuations, are also given in the following section. On the other hand, the relevant code and method have been verified in our previous work [35–43], in particular for detailed validations for stably and unstably stratified open channel flows based on DNS [35]. Thus, it is ensured that numerical approach is reliable to predict turbulence characteristics in the spanwise rotating channel.

4. Results and discussion

4.1. Mean turbulence statistics

The profiles of the mean velocity are shown in Fig. 3, where the bracket $\langle \rangle$ represents the average in time and in the horizontal plane. Based on the mean velocity profiles, the wall shear of rotating channel flow, compared to that

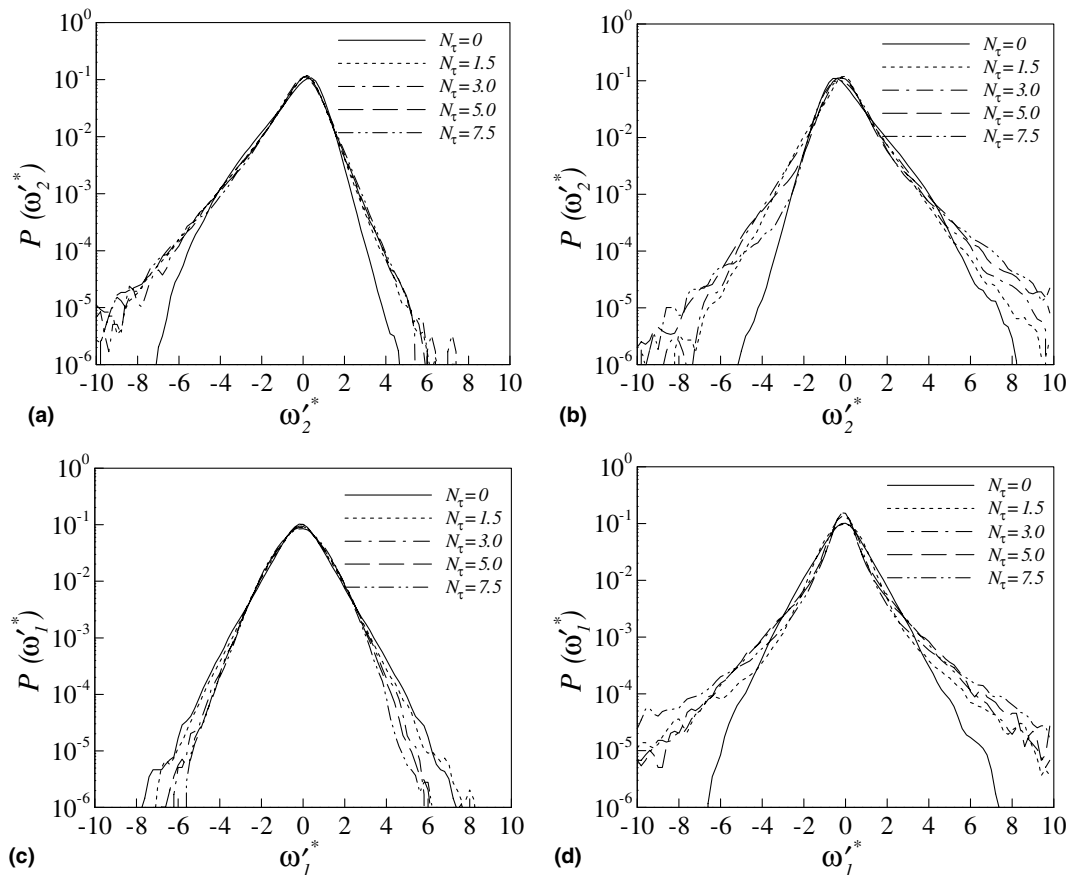


Fig. 7. PDF of the vorticity fluctuations at $z^+ = 5.8$: (a) ω'_2 in the pressure side, (b) ω'_2 in the suction side, (c) ω'_1 in the pressure side, (d) ω'_1 in the suction side. Here, the superscript '*' represents the quantity scaled by its root-mean-square value in the corresponding horizontal plane.

for $N_\tau = 0$, is enhanced near the pressure wall ($z/h = 1$) and reduced near the suction wall ($z/h = -1$), indicating the destabilization (or stabilization) of flow in the wall region near the pressure wall (or near the suction wall). Over the core region of the channel, the profiles of the mean velocities are approximately linear with the slope 2Ω , and the width of the region increases as N_τ increases, indicating the growth of irrotational zone with neutral stability. To validate the present calculations, as shown in Fig. 3, the present results agree well with the previous data [6,18].

Fig. 4 shows the turbulence intensities and the shear stress. An overall suppression of the turbulence intensities is observed near the suction wall ($z/h = -1$). The spanwise and wall-normal turbulence intensities (i.e., v'_{rms} and w'_{rms}) and the shear stress ($\langle u'w' \rangle$) are enhanced due to the Coriolis force effect near the pressure wall ($z/h = 1$). However, it is noted that the streamwise intensity u'_{rms} is somewhat augmented at low rotation number (e.g., $N_\tau = 1.5$) near the pressure wall, but greatly suppressed at high rotation number (e.g., $N_\tau = 7.5$), representing notable restability of turbulence near the pressure wall. This behavior is well consistent with the previous finding (see Fig. 7(a) in [6]) and is most likely associated with the growth of the irrotational zone, which penetrates far into the pressure side at high rotation rates. In this region, the induced Coriolis force

causes the near-wall flow to be neutrally stable and levels off the turbulence fluctuations. Furthermore, our calculated results in Fig. 4 are in good agreement with those [6,18].

4.2. Vorticity and wall streaks

As shown in Fig. 5(a) and (b), the streamwise vorticity fluctuation (ω'_{1rms}) exhibits enhancement near the pressure wall and suppression near the suction wall. At $N_\tau = 0$, there are a local minimum of ω'_{1rms} at $z^+ \approx 4.8$ and a maximum at $z^+ \approx 18$. As proposed by Kim et al. [18], a Rankine vortex model was used to explain the near-wall distribution of ω'_{1rms} in the non-rotating channel flow. The center of Rankine vortex corresponds to the position of local maximum of ω'_{1rms} and the size to the distance between the locations of local minimum and maximum of ω'_{1rms} . It is observed from Fig. 5(a) that, for the rotating flows, the location of local maximum of ω'_{1rms} shifts towards the pressure wall, and the distance between the locations of the minimum and maximum of ω'_{1rms} reduces as N_τ increases. This trend indicates that the size of the near-wall streamwise vortical structures becomes small. At $N_\tau = 7.5$, the local minimum and maximum of ω'_{1rms} near the pressure wall nearly disappears; it is attributed to a high gradient of ω'_{1rms} in the pressure wall region,

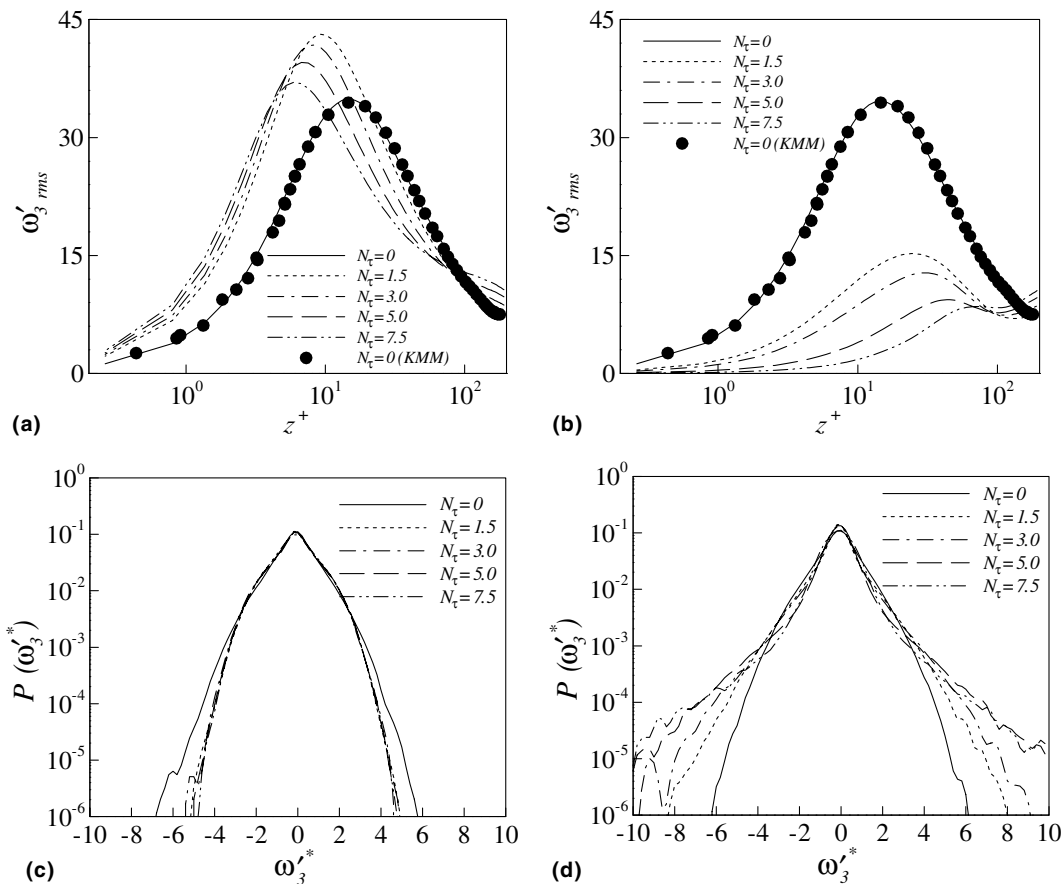


Fig. 8. Profiles of the wall-normal vorticity fluctuation and comparison with previous results as well as its PDF at $z^+ = 5.8$: (a) vorticity fluctuation in the pressure side, (b) vorticity fluctuation in the suction side, (c) PDF in the pressure side, (d) PDF in the suction side.

which results in a strong dynamic process to diffuse the streamwise vorticity fluctuation from the wall to the buffer layer. However, the distributions of ω'_{1rms} in Fig. 5(b) imply the appearance of large size streamwise vortical structure near the suction wall, and its center moves farther away from the suction wall as N_τ increases. Since ω'_{1rms} is related to the splattering effect of high-speed fluid rushing into the sublayer from buffer layer, the reduction of ω'_{1rms} near the suction wall thus corresponds to weakened splattering effect due to system rotation. In Fig. 5(b), a remarkable increase of ω'_{1rms} is depicted in the core region of the channel, especially in strong rotating case (e.g., $N_\tau = 7.5$). The behavior is ascribed to the presence of the large-scale roll cells in the rotating channel [6], which transport the streamwise vorticity fluctuation from the pressure side to the suction side, prevailing over the local decay of the streamwise vorticity fluctuation.

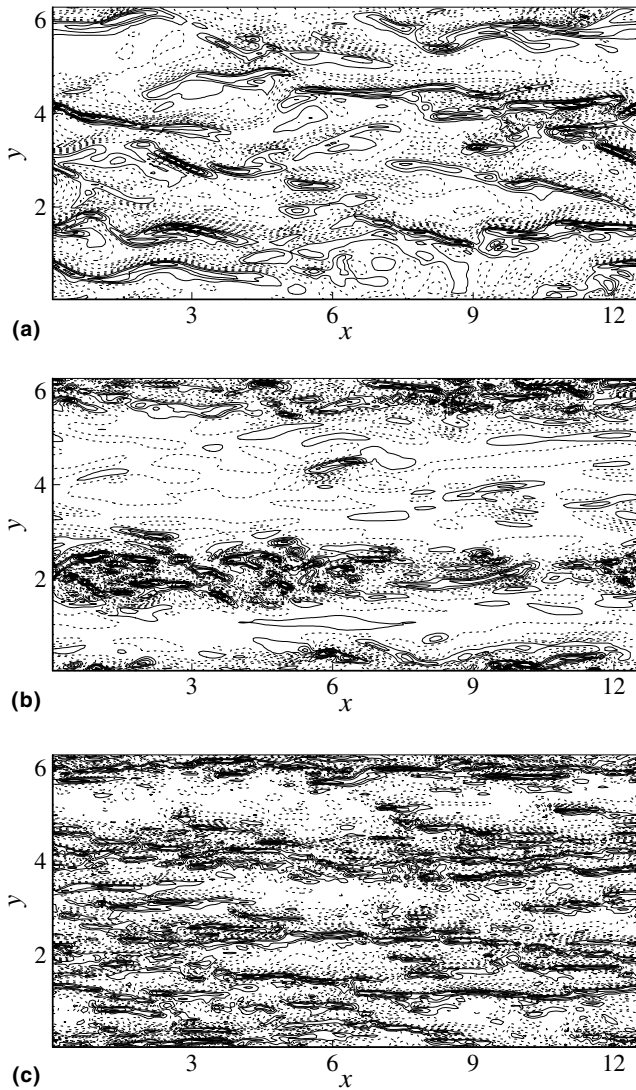


Fig. 9. Contours of the wall-normal vorticity fluctuation in (x, y) plane at $z^+ = 5.8$: (a) $N_\tau = 0$, (b) $N_\tau = 3.0$ in the suction side, (c) $N_\tau = 3.0$ in the pressure side. Here, contour increment $\Delta\omega'_3 = 0.7$.

The spanwise vorticity fluctuation ω'_{2rms} is shown in Fig. 5(c) and (d). Based on the definition, $\omega'_2 = \partial u'_1 / \partial x_3 - \partial u'_3 / \partial x_1$, the enhancement of ω'_{2rms} near the pressure wall is mainly due to the wall-normal gradient of u'_{1rms} increasing with the increase of N_τ in Fig. 4(a). In the pressure wall region, ω'_{2rms} decays rapidly in Fig. 5(c). However, as shown in Fig. 5(d), the distribution of ω'_{2rms} near the suction wall in strong rotation case (e.g., $N_\tau = 5$ and 7.5) is similar to that of ω'_{1rms} in the non-rotating case, where local minimum and maximum occur. It means that strong system rotation gives rise to the spanwise vortical structures with large size near the suction wall and is attributed to the spanwise wall shear flow related to the large-scale structures. At $N_\tau = 7.5$, ω'_{1rms} and ω'_{2rms} almost equal to each other in the suction wall region, indicating the weak wall shear of the relaminarized flow due to the rotation effect. Furthermore, the corresponding results predicted by Kim et al. [18] for $N_\tau = 0$ are given in Fig. 5; our calculated results agree well with the DNS data.

To exhibit the vortical structures in the wall regions, Fig. 6 shows the contours of vorticity fluctuations ω'_1 and ω'_2 in the (x, z) plane at $N_\tau = 3.0$. Since the wall coherent structures are closely related to turbulence events that generate the vorticity fluctuations by vortex stretching effects, it is indicated in Fig. 6 that the vortex stretching effect is

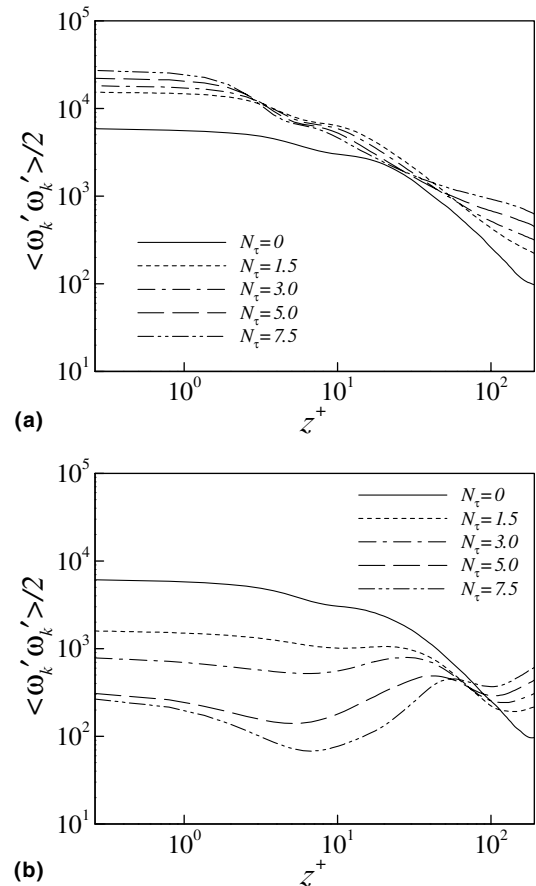


Fig. 10. Distributions of $\langle \omega'_k \omega'_k \rangle / 2$: (a) in the pressure side, (b) in the suction side.

enhanced near the pressure wall and reduced near the suction wall. The suppression of the vortical structures in the suction wall region is responsible for the reduction of turbulence intensities. The enhancement of the streamwise vortical structures near the pressure wall is associated with the increase of the vortex stretching and turbulence production.

To get insight into the modification of near-wall vortical structures subject to system rotation, Fig. 7 shows the PDF of ω'_2 . It is seen that the PDF profiles of ω'_2 are not symmetric about $\omega'_2 = 0$ in the wall regions; negative ω'_2 is predominant near the pressure wall in Fig. 7(a) while positive ω'_2 predominant near the suction wall in Fig. 7(b). The behavior is consistent with the near-wall distribution of the mean spanwise vorticity. In the rotating cases, Fig. 7(b) exhibits a remarkable increase of the probability of negative ω'_2 but a small change of the probability of positive ω'_2 . This trend leads to the shape of the PDF profile of ω'_2 somewhat more symmetric about $\omega'_2 = 0$ and is associated with the suppression of ω'_{2rms} near the suction wall. In Fig. 7(c) and (d), the PDF profiles of ω'_1 are nearly symmetric about $\omega'_1 = 0$, accounting for zero mean streamwise vorticity in the wall regions. The probability of ω'_1 exhibits a tendency to zero in the pressure wall region, but to extensive negative and positive value in the suction wall region. This behavior indicates the more intermittent flow occurs near the suction wall due to rotation effect. As the spanwise component of mean vorticity, i.e., $\langle \omega_2 \rangle$, is non-zero, the tendency of the PDF of ω'_2 to be more symmetric distribution reflects the suppression of the vortical structures near the suction wall.

Fig. 8(a) and (b) shows the profiles of the wall-normal vorticity fluctuation ω'_{3rms} . An overall suppression of ω'_{3rms} near the suction wall can be observed. However, in the pressure wall region, it is interesting to note that, unlike ω'_{1rms} and ω'_{2rms} , ω'_{3rms} is no longer monotonously enhanced with N_τ . As shown in Fig. 8(a), ω'_{3rms} increases up to $N_\tau = 1.5$, then decreases as N_τ increases further. According to the definition of ω'_3 , i.e., $\omega'_3 = \partial u'_2 / \partial x_1 - \partial u'_1 / \partial x_2$, the behavior is ascribed to the change of the streamwise turbulence intensity u'_{rms} near the pressure wall shown in Fig. 4(a). The corresponding results predicted by Kim et al. [18] at $N_\tau = 0$ are given in Fig. 8(a) and (b) for comparison. Further, it is viewed from Fig. 8(c) and (d) that the PDF profile of ω_3 is nearly symmetric distribution about $\omega'_3 = 0$, even in the rotating cases.

Contours of ω'_3 in the (x, y) plane at $z^+ = 5.8$ are shown in Fig. 9 for $N_\tau = 0$ and 3.0. By comparing with the structures in Fig. 9(a) for $N_\tau = 0$, the vorticity fluctuation ω'_3 near the pressure wall in Fig. 9(c) becomes stronger with smaller spanwise spacing. Correspondingly, the contours of ω'_3 near the suction wall in Fig. 9(b) are concentrated into two narrow zones aligned in the streamwise direction. This pattern is ascribed to the appearance of two pairs of large-scale Taylor–Görtler-like structures [6], transporting the velocity and vorticity fluctuations from the pressure side to the suction side.

The enstrophy is associated with the motion of small scales, i.e., dissipating eddies; the region with high dissipation usually corresponds to that with high value vorticity, as implied by the relation between the dissipation rate and fluctuating enstrophy,

$$\varepsilon = -\frac{1}{Re_\tau} \frac{\partial u'_i}{\partial x'_j} \frac{\partial u'_i}{\partial x'_j} = -\frac{1}{Re_\tau} \left(s'_{ij} s'_{ij} + \frac{\omega'_k \omega'_k}{2} \right) \quad (4)$$

where ε denotes the dissipation rate and $s'_{ij} = (\partial u'_i / \partial x'_j + \partial u'_j / \partial x'_i) / 2$. As shown in Fig. 10 for the profiles of $\langle \omega'_k \omega'_k \rangle / 2$, the motion of small eddies is more active near the pressure wall, and the turbulence is thus expected to be in high dissipation level. While near the suction wall, the dissipating eddies is monotonously suppressed as N_τ increases.

4.3. Fluctuating Lamb vector and turbulence production

The transport equation of turbulent kinetic energy $k = \langle u'_i u'_i \rangle / 2$, derived from the Navier–Stokes equations in rotational form, is written as

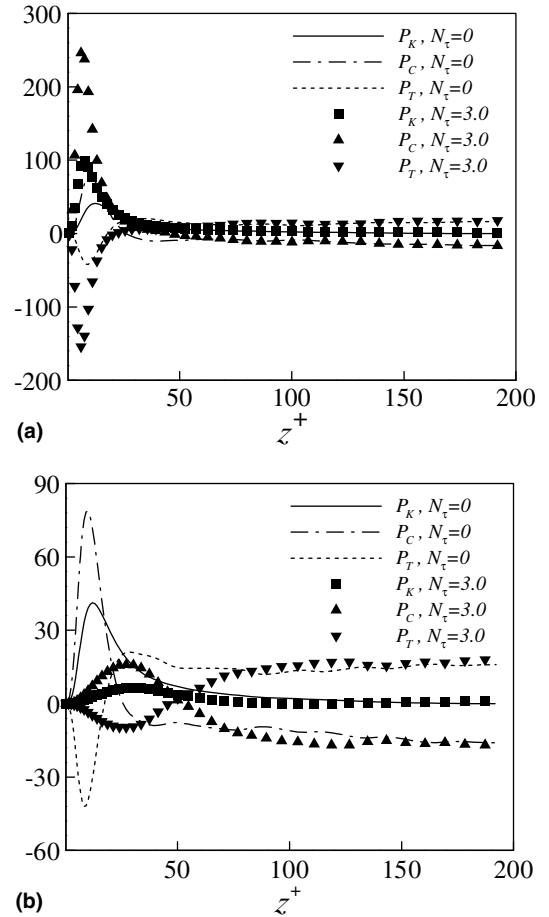


Fig. 11. Contributions of P_T and P_C to P_K at $N_\tau = 0$ and $N_\tau = 3.0$: (a) in the pressure side, (b) in the suction side.

$$\begin{aligned} \frac{\partial k}{\partial t} + \varepsilon_{ijk} \langle u_k \rangle \langle \omega'_j u'_i \rangle + \frac{\partial \langle u_k \rangle \langle u'_i u'_k \rangle}{\partial x_i} \\ = - \frac{\partial \langle \phi' u'_i \rangle}{\partial x_i} + \frac{1}{Re_\tau} \frac{\partial k}{\partial x_j \partial x_j} + \varepsilon \end{aligned} \quad (5)$$

where ϕ' denotes the fluctuating enthalpy, $\phi' = p' + u'_i u'_i / 2$, ε is the dissipation rate. Based on Eqs. (5) and (A.1) in Appendix A, we reach

$$\begin{aligned} - \left[\langle u'_i u'_k \rangle \frac{\partial \langle u_i \rangle}{\partial x_k} + \frac{1}{2} \langle u_k \rangle \frac{\partial \langle u'_i u'_i \rangle}{\partial x_k} \right] \\ = - \left[\varepsilon_{ijk} \langle u_k \rangle \langle \omega'_j u'_i \rangle + \frac{\partial \langle u_k \rangle \langle u'_i u'_k \rangle}{\partial x_i} \right] \end{aligned} \quad (6)$$

Here, both the terms on the left-hand side (LHS) represent the production rate and mean flow convection term for the turbulence kinetic energy, respectively. In Eq. (6), it means that the fluctuating Lamb vector $\gamma'_k = \varepsilon_{ijk} \omega'_j u'_i$ involves the turbulent kinetic energy production. The first term on the right-hand side (RHS) of Eq. (6) is related to the energy cascade from large to small scales, and the second one to the motion of large-scale eddies advecting turbulence energy [44]. As a fully developed turbulence flow in the rotating channel is assumed, Eq. (6) can be simplified as

$$- \langle u'_1 u'_3 \rangle \frac{\partial \langle u_1 \rangle}{\partial x_3} = - \left[\langle u_1 \rangle (\langle \omega'_3 u'_2 \rangle - \langle \omega'_2 u'_3 \rangle) + \frac{\partial \langle u_1 \rangle \langle u'_1 u'_3 \rangle}{\partial x_3} \right] \quad (7)$$

which reflects that only the streamwise component of $\vec{\gamma}'$, i.e., $\gamma'_1 = \langle \omega'_3 u'_2 \rangle - \langle \omega'_2 u'_3 \rangle$, contributes to the turbulent energy production. The difference between the energy gained by the advection of large eddies and the energy cascaded to small scales is the net contribution to turbulent kinetic energy production. For convenience, these three terms in Eq. (7) are denoted by P_K (i.e., term on LHS), P_T (first term on RHS) and P_C (second term on RHS), respectively.

To reveal the influence of system rotation on the near-wall turbulence energy production, Fig. 11 shows the profiles of P_K , P_T and P_C at $N_\tau = 0$ and 3. In the pressure wall region (Fig. 11(a)), the turbulent flow gets more energy by the advection of large eddies, resulting in more energetic turbulence in the rotating case. However, in the suction wall region (Fig. 11(b)), the motion of large eddies is suppressed. It is noted that P_C changes its sign to be negative in the center of the channel, which implies the dynamic process that large eddies transport energy from the turbulent flow to the mean motion.

The profiles of P_K are shown in Fig. 12(a) and (b). The difference between P_C and P_T gives positive contribution to the turbulence energy production. Due to the effect of rotation, the reduction of shear stress $-\langle u'_1 u'_3 \rangle$ and the shear rate of mean flow (i.e., $d\langle u \rangle/dz$) leads to the suppression of turbulence energy production in the suction wall region. In Fig. 12(a), the higher peak value of P_K is responsible for the local maximum of u'_{rms} near the pressure wall in

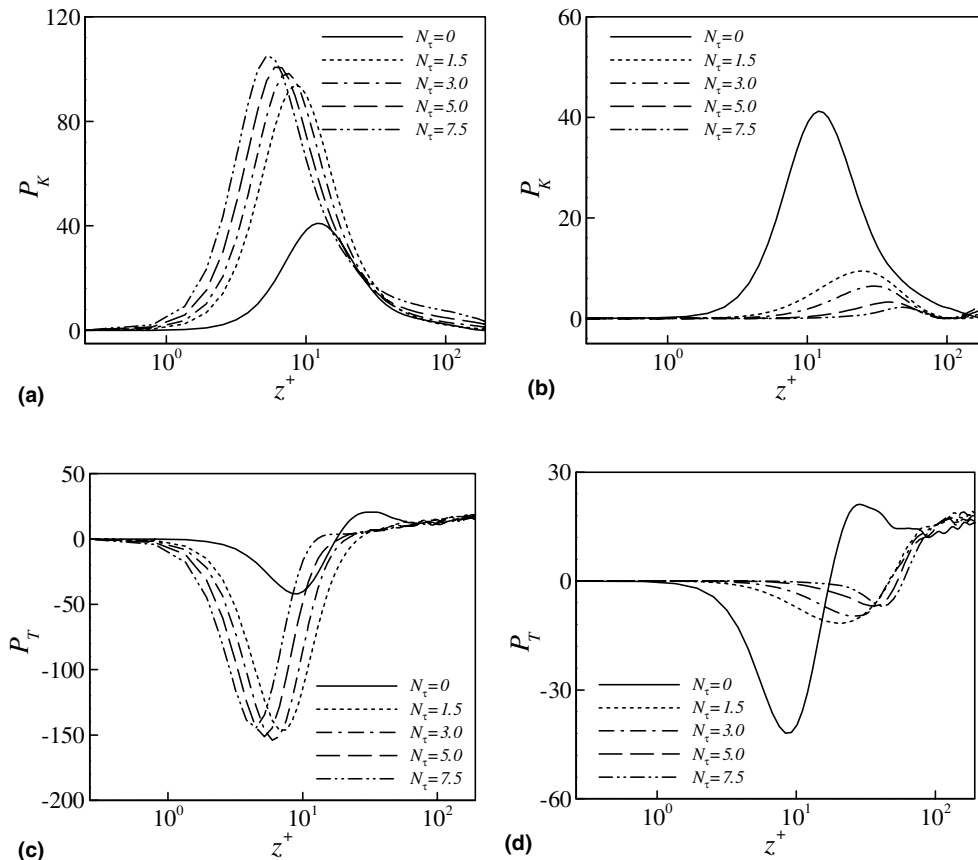


Fig. 12. Profiles of P_K and P_T : (a) P_K in the pressure side, (b) P_K in the suction side, (c) P_T in the pressure side, (d) P_T in the suction side.

Fig. 4(a). In the core region, P_K is the offset between the energy cascaded to small scales and the energy obtained by the advection of large eddies. As shown in Fig. 12(c) and (d), the negative P_T in the near wall regions indicates that small-scale motions drain energy from large-scale ones, and the positive P_T in the core region implies the inverse energy cascade from small scales to large ones. Similar behavior was also found in the rotating pipe flow [11].

As shown in Fig. 13 for the profiles of the streamwise component of fluctuating Lamb vector γ'_1 , the reduction of γ'_1 near the suction wall is a key factor to rapid drop of P_T as N_τ increases. Thus, system rotation prevents the energy cascade from large to small scales, leading to the turbulence leveling off near the suction wall. The sign of γ'_1 reverses in the core region in Fig. 13(b), accounting for the inverse energy cascade from small to large scales there. Correspondingly, the enhancement of γ'_1 near the pressure wall is identified in Fig. 13(a).

Fig. 14 shows the PDF of γ'_1 , by taking an average in the (x, y) plane at $z^+ = 5.8$ and scaled by the mean value of $\langle (u'_i u'_i)^{1/2} (\omega'_i \omega'_i)^{1/2} \rangle$ in the same plane. The probability

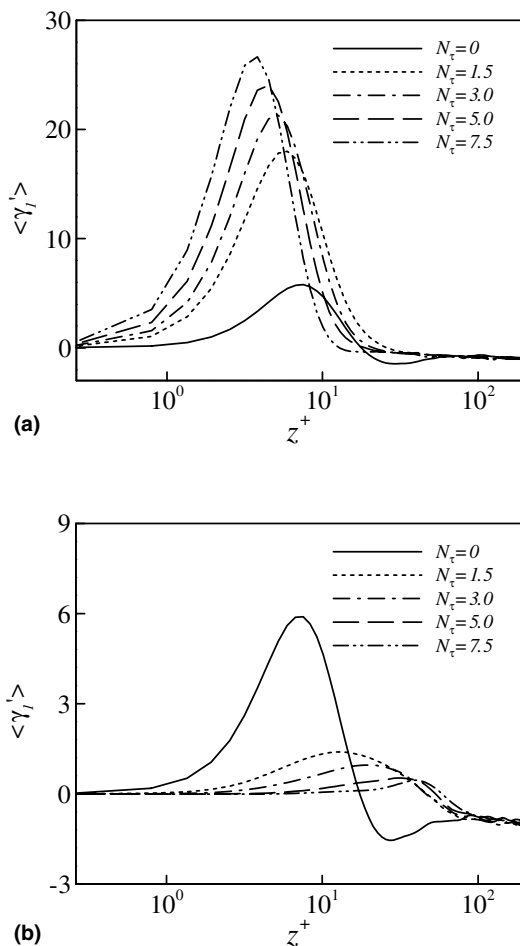


Fig. 13. Distributions of the streamwise component of Lamb vector fluctuation $\langle \gamma'_1 \rangle$: (a) in the pressure side, (b) in the suction side.

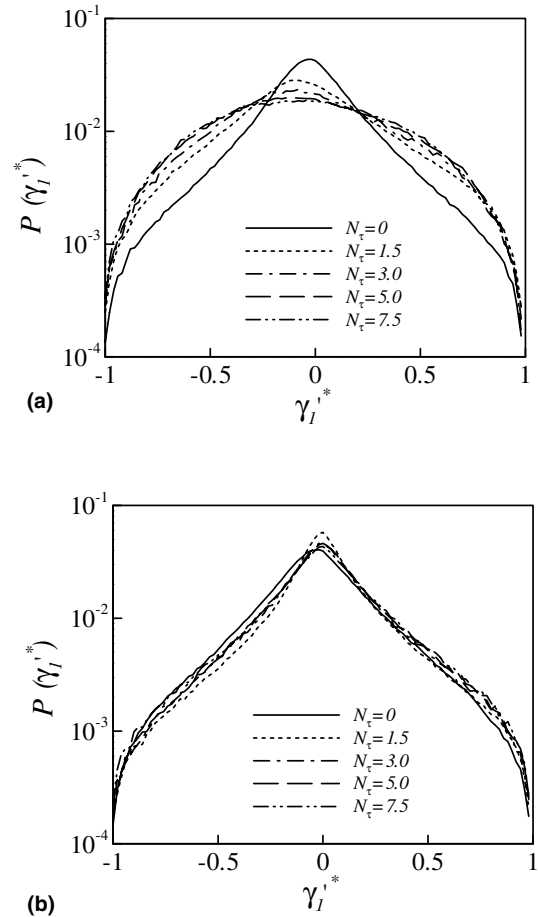


Fig. 14. PDF of γ'_1 at $z^+ = 5.8$: (a) in the pressure side, (b) in the suction side.

of γ'_1 to be negative increases somewhat near the pressure wall in Fig. 14(a), and the shape of the PDF profiles of γ'_1 is no longer symmetric about the axis $\gamma'_1 = 0$. However, the shape of the PDF profiles of γ'_1 exhibits little alteration near the suction wall in Fig. 14(b). Thus, it is reasonably predicted that the enhancement of γ'_1 close to the pressure wall is related to the trend of the PDF distribution of γ'_1 .

To dissect the behavior of γ'_1 , both terms $\langle u'_3 \omega'_2 \rangle$ and $\langle u'_2 \omega'_3 \rangle$ are shown in Fig. 15. The enhancement of positive γ'_1 in the sublayer close to the pressure wall is mainly due to the augmentation of positive $\langle u'_2 \omega'_3 \rangle$, which indicates higher correlation between the spanwise velocity fluctuation generated by the splattering effect and the rotation-enhanced normal vorticity fluctuation. The term $\langle u'_3 \omega'_2 \rangle$ is also responsible for appreciable positive contribution to γ'_1 in the region of $z^+ > 10$. This correlation is related to the ejection and sweep events, which produces elongated high- and low-speed wall streaks and reduces the spanwise spacing of the wall streaky structures. In the suction wall region, remarkable reduction of γ'_1 results from the suppression of turbulence burst events generating turbulence fluctuations and vortical structures.

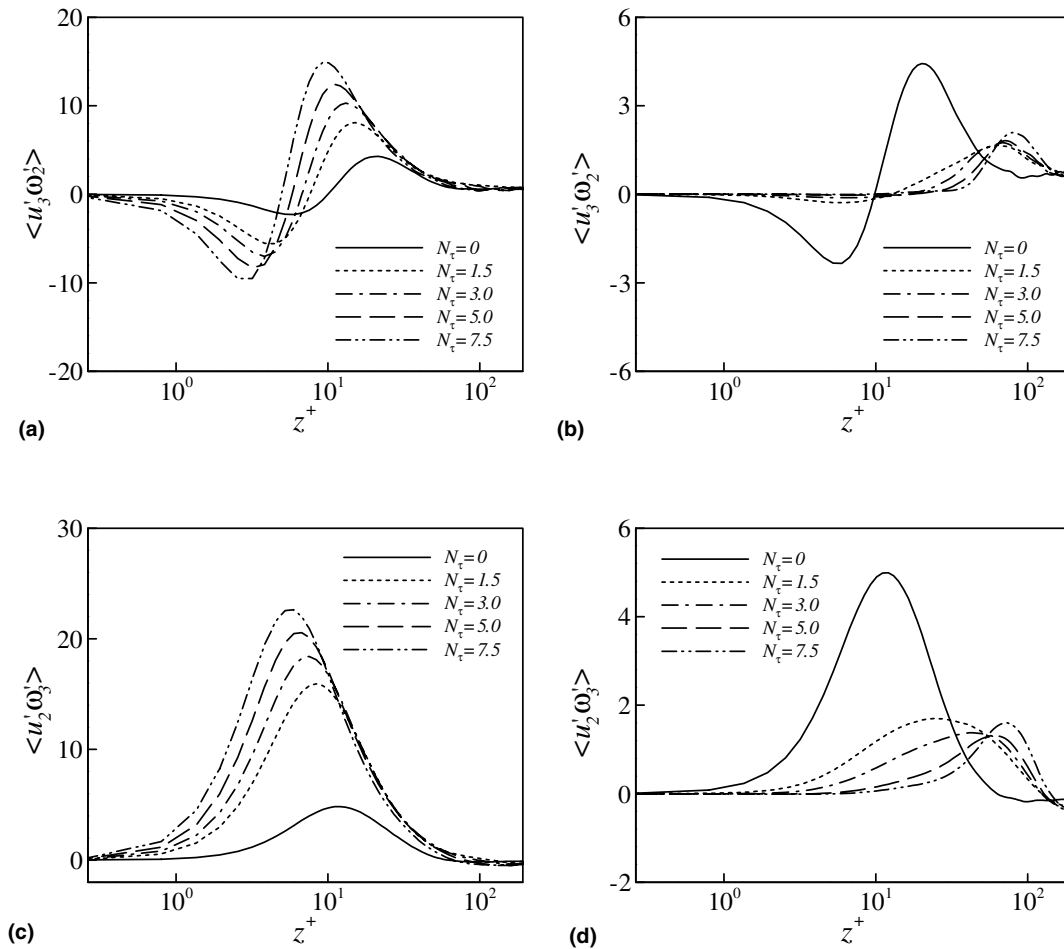


Fig. 15. Profiles of the correlation between fluctuating velocity and vorticity component: (a) $\langle u'_3\omega'_2 \rangle$ in the pressure side, (b) $\langle u'_3\omega'_2 \rangle$ in the suction side, (c) $\langle u'_2\omega'_3 \rangle$ in the pressure side, (d) $\langle u'_2\omega'_3 \rangle$ in the suction side.

4.4. Turbulence budgets

To examine the influence of rotation on the turbulence budgets, in particular in the wall regions, dynamical characteristics of turbulence based on the production rate, redistribution and dissipation rate of turbulent kinetic energy, referred to Eq. (A.1) in Appendix A, is analyzed here.

The budget terms of $\langle u'u' \rangle$ at $N_\tau = 0$ and 7.5 are shown in Fig. 16. Compared to the non-rotating case in Fig. 16(a), the damping of the production rate P_{11} (i.e., PR) in the suction wall region in Fig. 16(c) is ascribed to the suppression of $\langle u'w' \rangle$ shown in Fig. 4(d). The peak of P_{11} shifts towards the pressure wall, where the process of turbulence production is more active in the rotating cases. In the immediate vicinity of the pressure wall, the balance of $\langle u'u' \rangle$ budget is mainly due to the interaction between the viscous diffusion D_{11} (i.e., VD) and dissipation rate ε_{11} (i.e., DS). The negative pressure strain correlation π_{11} (i.e., PS) represents the turbulence energy redistribution from the streamwise velocity fluctuation to the spanwise and wall-normal components in the wall regions. Fig. 16(c) exhibits that π_{11} changes to be positive in the core region at $N_\tau = 7.5$, which implies an inverse turbulence energy redistribution from the

other two components to the streamwise fluctuation component. It is noted that the Coriolis force velocity correlation N_{11} (i.e., CO) becomes comparable to P_{11} in the core region. In the pressure wall region, P_{11} becomes more active at $z^+ \approx 5.6$ in Fig. 16(b), corresponding to the maximum of u'_{rms} in Fig. 4(a). As shown in Fig. 17 for the profiles of N_{11} , negative N_{11} is enhanced in the most region of the channel and acts as a sink term in the $\langle u'u' \rangle$ budget as π_{11} does.

The budget terms of $\langle w'w' \rangle$ are shown in Fig. 18. Since the wall-normal mean velocity is zero, the production term in the $\langle w'w' \rangle$ budget is trivial. In the non-rotating case (Fig. 18(a)), the pressure strain correlation π_{33} (i.e., PS) and the pressure–velocity diffusion Π_{33} (i.e., PV) play as the dominant terms, which are responsible for the turbulence energy redistribution from the streamwise to wall-normal fluctuation. In the rotating case, Fig. 18(b) shows that the Coriolis force velocity correlation N_{33} (i.e., CO) is appreciably enhanced and becomes a dominant term in the $\langle w'w' \rangle$ budget in the core region. However, since $N_{22} = 0$ and $N_{11} + N_{33} = 0$, as indicated in Eq. (5), system rotation gives null contribution to the generation of turbulent kinetic energy. Remarkably positive value of N_{33} in the core region represents that N_{33} acts as a role to redistribute

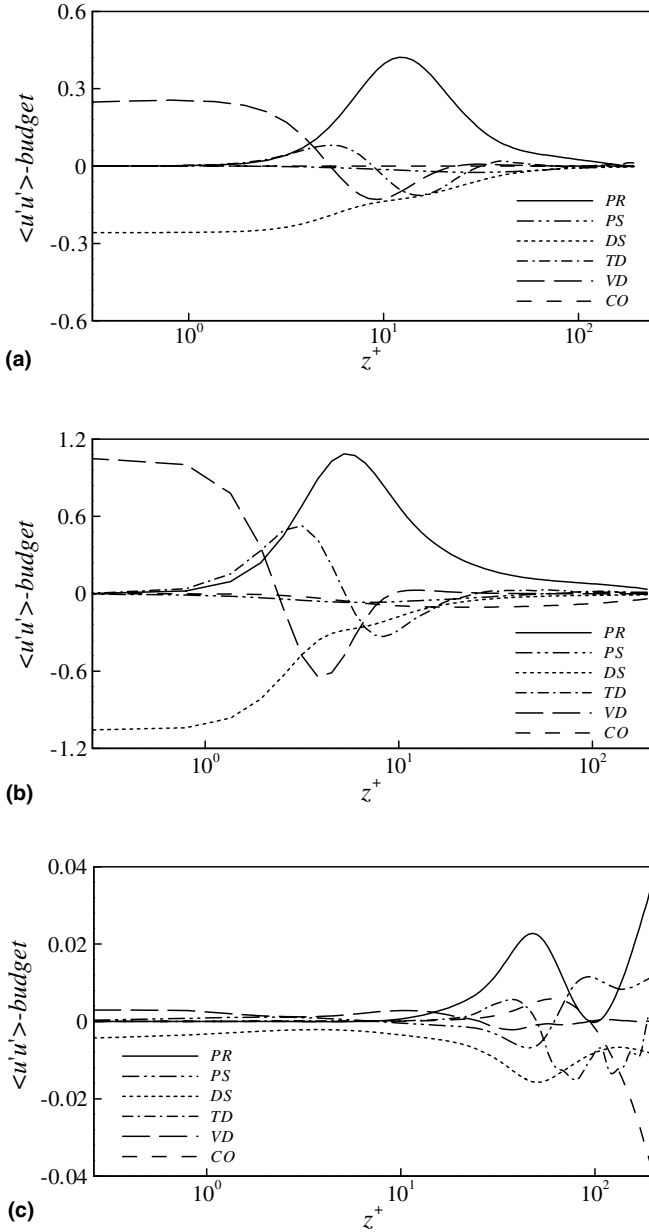


Fig. 16. Budgets of streamwise turbulence kinetic energy $\langle u'u' \rangle$: (a) $N_\tau = 0$, (b) $N_\tau = 7.5$ in the pressure side, (c) $N_\tau = 7.5$ in the suction side.

the turbulent energy among the turbulence fluctuations. An overview on the N_{11} and N_{33} is that the Coriolis force term contributes to the turbulent kinetic energy redistribution from the streamwise to wall-normal component.

Fig. 19 shows the budget terms of $\langle u'w' \rangle$. In the close wall regions, only the pressure strain correlation π_{13} (i.e., PS) and the pressure–velocity diffusion Π_{13} (i.e., PV) contribute to the budget of $\langle u'w' \rangle$ in Fig. 19(a). The production rate P_{13} (i.e., PR) is the primary source term in $z^+ > 10$. In Fig. 19(b) and (c), it is noted that the positive Coriolis force velocity correlation N_{13} (i.e., CO) becomes comparable to P_{13} in the near wall regions. Thus, N_{13} acts as a major source term near the walls in the budget of $\langle u'w' \rangle$, but a sink term in the core region to balance P_{13} . Furthermore,

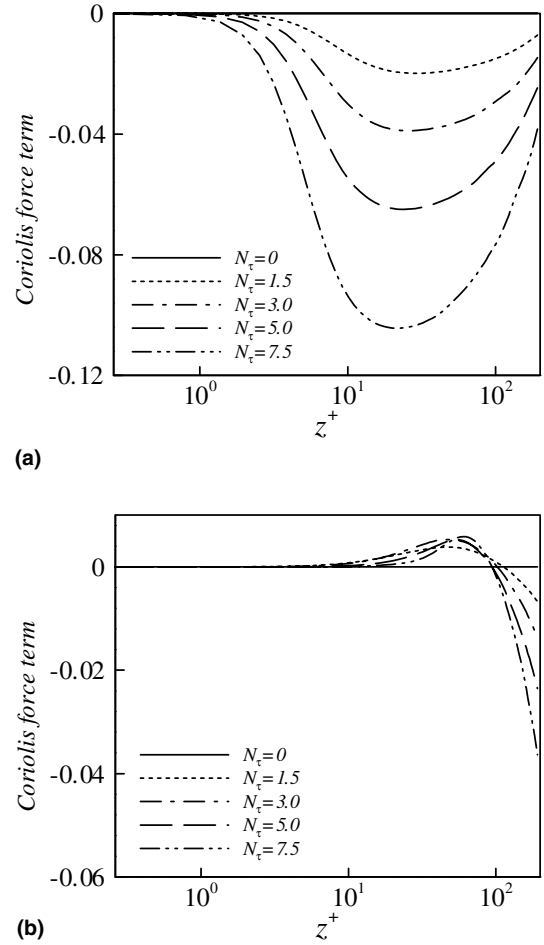


Fig. 17. Profiles of the Coriolis force velocity correlation term N_{11} : (a) in the pressure side, (b) in the suction side.

Fig. 20 shows the profiles of N_{13} . It is seen that the sign of N_{13} reverses twice over the channel. Based on the definition $N_{13} = N_\tau(\langle u'_1 u'_1 \rangle - \langle u'_3 u'_3 \rangle)$, it is reasonably predicted that the sign reversion of N_{13} is resulted from the distributions of $\langle u'_1 u'_1 \rangle$ and $\langle u'_3 u'_3 \rangle$ shown in Fig. 4(a) and (c), respectively. Since $\langle u'w' \rangle$ is closely connected with the near-wall streamwise vortices, the distributions of N_{13} in Fig. 20 indicate the vortex stretching being augmented near the pressure wall and damped near the suction wall.

An overview on the budgets of $\langle u'u' \rangle$, $\langle w'w' \rangle$ and $\langle u'w' \rangle$ is that the Coriolis force makes null contribution to the generation of turbulent kinetic energy, but acts as an important role to redistribute the turbulent kinetic energy from the streamwise to wall-normal turbulence fluctuations and to influence vortex stretching in the wall regions.

4.5. Fluctuating enstrophy budget

To reveal the behaviors of the fluctuating enstrophy budget, the transport equation for the fluctuating enstrophy is given in Eq. (A.2) in Appendix A. Usually PR^{GR} plays a role to exchange enstrophy between the mean and fluctuating vorticity field, and PR^{MV} and PR^{TV} are

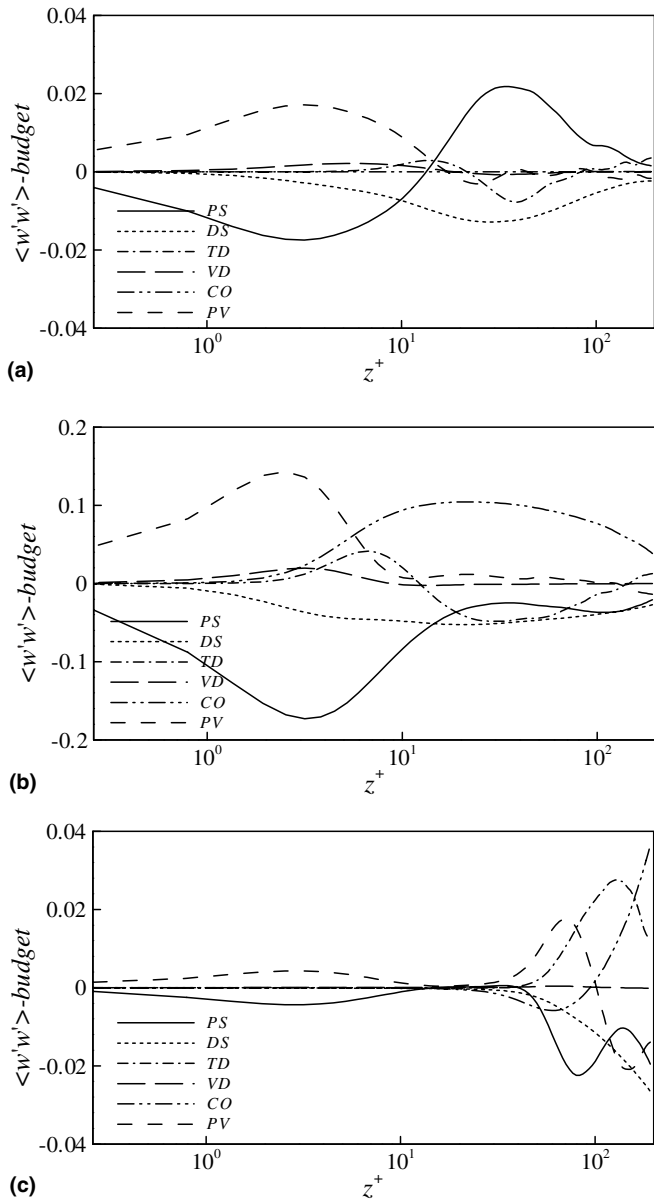


Fig. 18. Budgets of normal turbulence kinetic energy $\langle w'w' \rangle$: (a) $N_\tau = 0$, (b) $N_\tau = 7.5$ in the pressure side, (c) $N_\tau = 7.5$ in the suction side.

responsible for the vortex stretching and distortion of fluctuating vorticity induced by the mean and fluctuating velocity field, respectively. Here, our attention is mainly paid on the production terms to reveal the mechanism of vortex stretching near the pressure and suction walls.

The budget terms of the fluctuating enstrophy $\langle \omega'_i \omega'_i \rangle / 2$ at $N_\tau = 0$ and 3 are shown in Fig. 21. It is exhibited that both PR^{GR} and PR^{RM} are negligibly small compared to other production terms. Thus, the dynamic process to exchange vorticity from large-scale vortices to fluctuating vortices is weak. The terms PR^{TV} , PR^{MV} and PR^{MM} are the dominant ones to the $\langle \omega'_i \omega'_i \rangle / 2$ budget. It is noted that PR^{MM} is the largest production term near the pressure wall in Fig. 22(b), which indicates that the fluctuating enstrophy is mainly produced by the stretching and distortion of mean

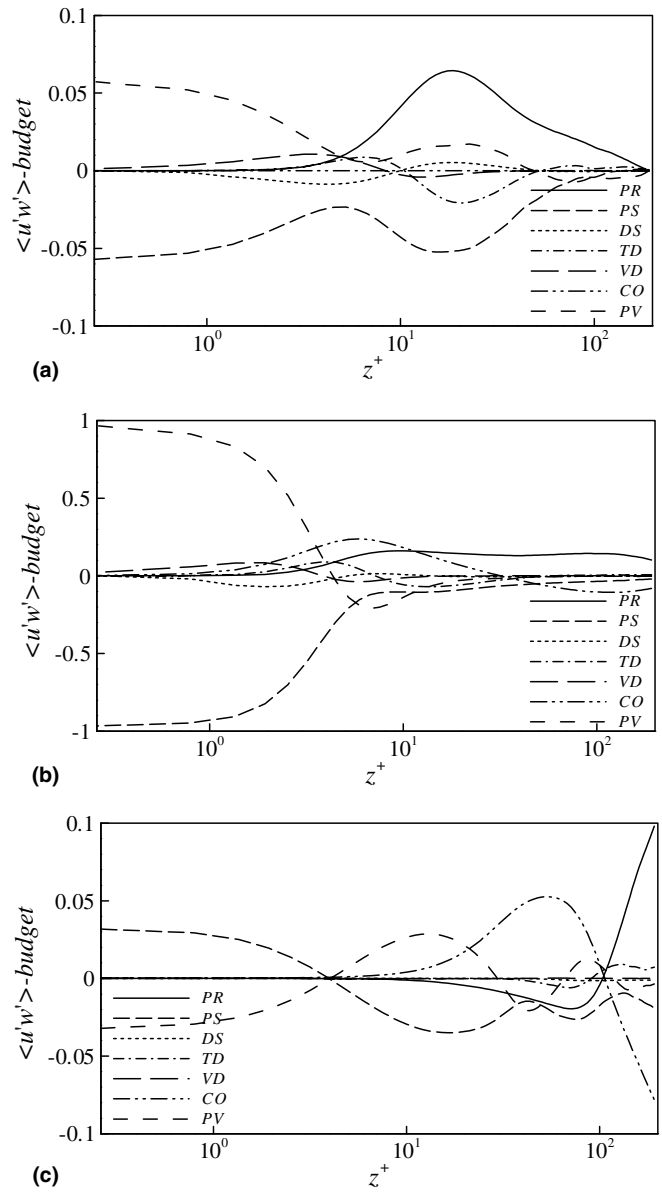


Fig. 19. Budgets of Reynolds stress $\langle u'w' \rangle$: (a) $N_\tau = 0$, (b) $N_\tau = 7.5$ in the pressure side, (c) $N_\tau = 7.5$ in the suction side.

vorticity (i.e., $\langle \omega_2 \rangle$ for the channel flow) induced by the strain rate of fluctuating velocity field. Compared to the non-rotating case in Fig. 21(a), the contribution of PR^{MV} becomes less important to the $\langle \omega'_i \omega'_i \rangle / 2$ budget in Fig. 21(b). However, as shown in Fig. 21(c), both terms PR^{TV} and PR^{MV} prevail over PR^{MM} and become important production terms in the suction wall region, indicating that the process of fluctuating vorticity stretching induced by the fluctuating velocity field, i.e., PR^{TV} , contributes the most to the generation of fluctuating enstrophy, so does the distortion of fluctuating vorticity due to the mean flow shear, i.e., PR^{MV} .

Fig. 22 shows the profiles of PR^{TV} , PR^{MV} , PR^{MM} and VD terms. An overview on these production terms is the rotational alteration of vortex stretching, significantly enhanced near the pressure wall and suppressed near the

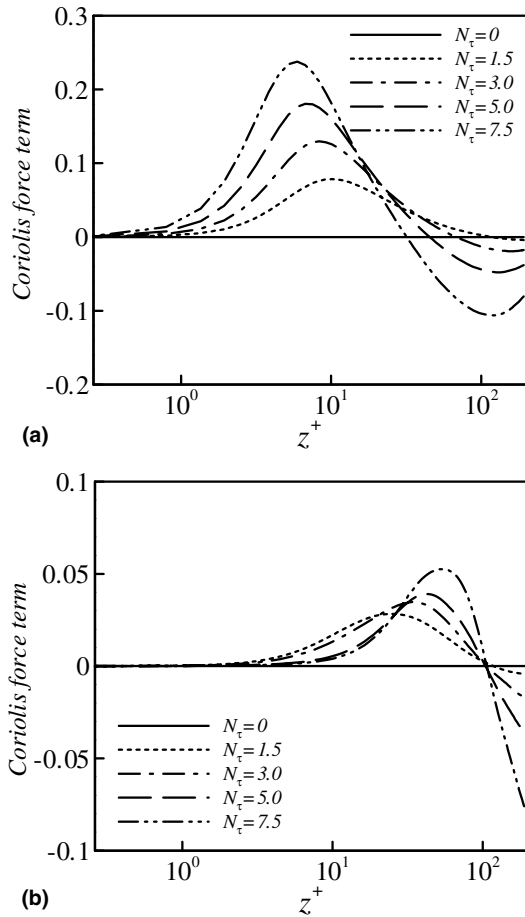


Fig. 20. Profiles of the Coriolis force velocity correlation term N_{13} : (a) in the pressure side, (b) in the suction side.

suction wall. It is noted that the distributions of PR^{TV} , PR^{MV} and PR^{MM} terms close to the suction and pressure walls are similar to these in the channel flows at low and high Reynolds number [23]. This similarity is due to the fact that, if scaled by the local friction velocity at the suction or pressure wall, the Reynolds number near the suction wall is lower than that near the pressure wall [6]. In the non-rotating case, there appear two local maximums in the profile of PR^{TV} , at $z^+ = 3$ and $z^+ = 11$ in Fig. 22(a); in the rotating cases, however, only one maximum is notable in the wall regions. As shown in Fig. 22(a) and (c), the peaks of PR^{TV} and PR^{GR} locate in the region $z^+ < 15$; it means that more active processes of vorticity stretching induced by the fluctuating velocity field occur in the sub-layer. The term PR^{MV} acts as a dominate term due to the mean flow shear in Fig. 22(b). The negative viscous diffusion term VD in Fig. 22(d) reflects that, due to the viscous diffusion effect, the vorticity fluctuations are transported away from the pressure wall to the buffer region and to the core region shown in Fig. 5(a). In the suction wall region, the sign of VD still keeps positive. It means that the rotation effect induces different roles of the viscous diffusion near the pressure and suction walls.

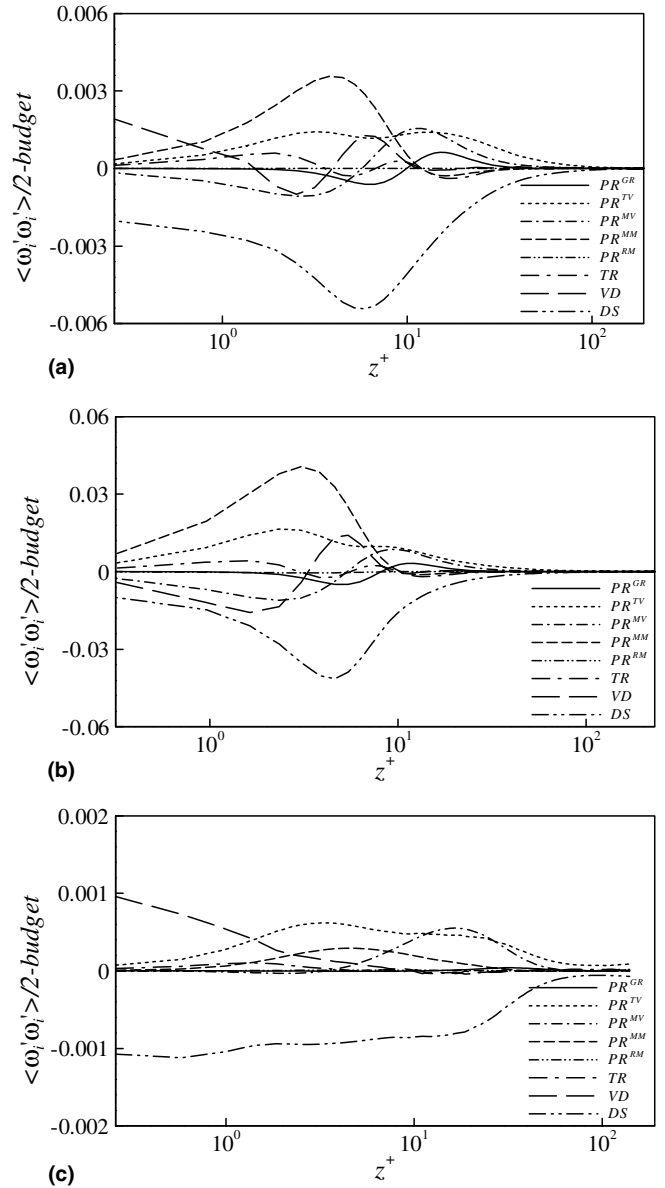


Fig. 21. Budgets of fluctuating enstrophy $\langle \omega_i' \omega_i' \rangle / 2$: (a) $N_\tau = 0$, (b) $N_\tau = 3.0$ in the pressure side, (c) $N_\tau = 3.0$ in the suction side.

5. Concluding remarks

A fully developed turbulent flow in a spanwise rotating channel is studied by solving the three-dimensional incompressible Navier–Stokes equations. Turbulence characteristics subject to system rotation, including the near-wall vortical structures, turbulence energy cascade and redistribution, and the budgets of Reynolds stresses and fluctuating enstrophy, are investigated. The near-wall vortical structures are suppressed near the suction wall and augmented near the pressure wall. The rotational-dependent alteration of the PDF profiles is identified according to the PDF profiles of the vorticity fluctuations in the pressure and suction wall regions. The influence of system rotation on energy

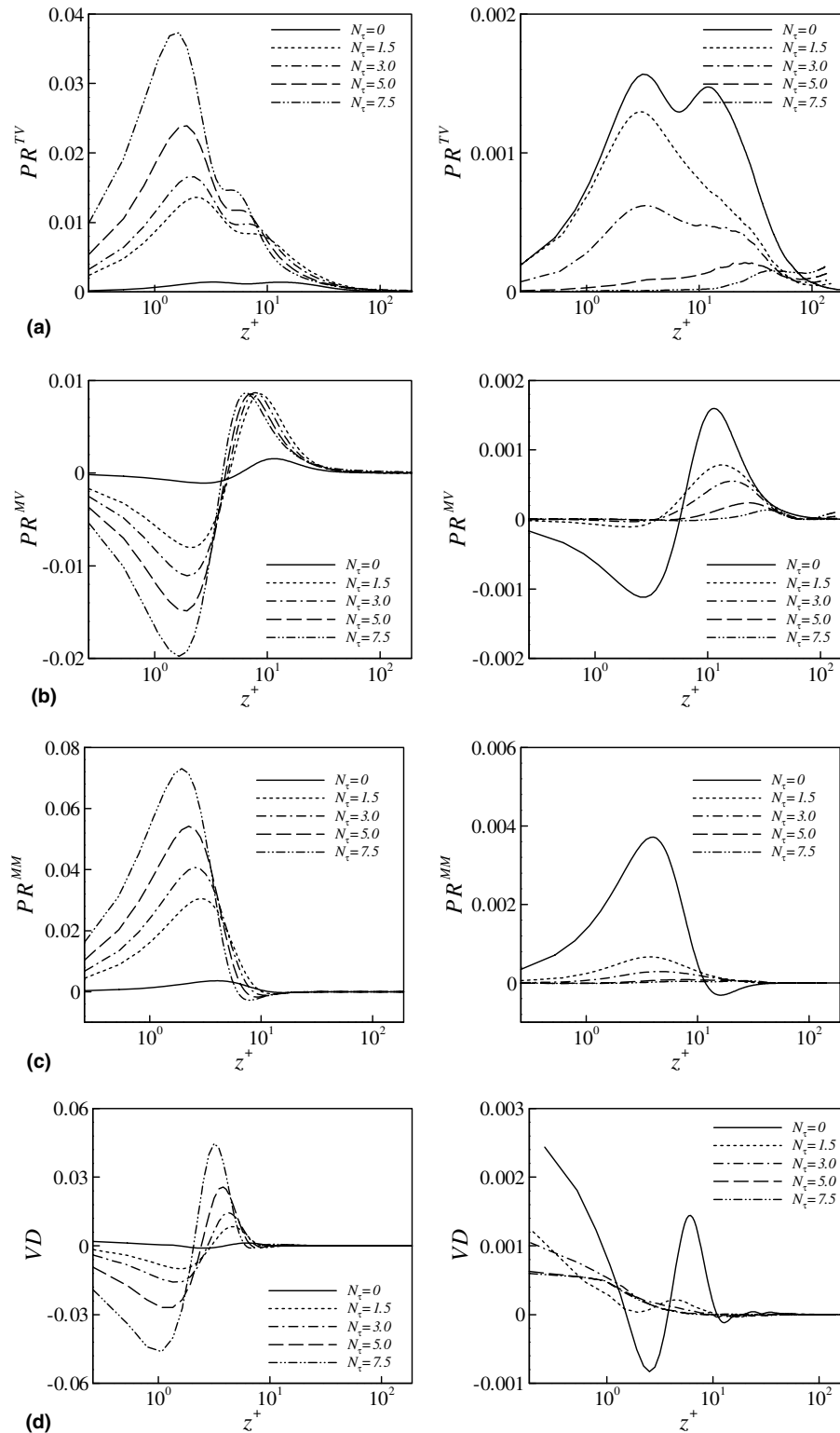


Fig. 22. Budget terms of fluctuating enstrophy in the pressure side (left column) and suction side (right column): (a) PR^{TV} , (b) PR^{MV} , (c) PR^{MM} , (d) VD .

cascade from large to small scales in the wall regions is revealed based on the streamwise component of Lamb vector fluctuation. The budgets of Reynolds stresses exhibit that the turbulence energy production and redistribution are activated near the pressure wall and suppressed near the suction wall. The energy redistribution due to the Cori-

olis force plays as an important role as the rotation rate increases. Based on examining the terms relevant to the fluctuating enstrophy production in the budget equation, there exist different vortex stretching mechanisms for the generation of the fluctuating vorticity in the pressure and suction wall regions.

Acknowledgements

This work was supported by the National Natural Science Foundation of China (Nos. 10302028, 90405007, 10125210), the Hundred Talents Program of the Chinese Academy of Sciences, and Specialized Research Fund for the Doctoral Program of Higher Education (No. 20020358013).

Appendix A. Equations for statistical quantities

The transport equation for the Reynolds stresses is

$$\frac{\partial \langle u'_i u'_j \rangle}{\partial t} + \langle u_k \rangle \frac{\partial \langle u'_i u'_j \rangle}{\partial x_k} = P_{ij} + T_{ij} + D_{ij} + \Pi_{ij} + \pi_{ij} + \varepsilon_{ij} + N_{ij} \quad (\text{A.1})$$

where the terms on the right-hand side are

$P_{ij} = - \left[\langle u'_i u'_k \rangle \frac{\partial \langle u_j \rangle}{\partial x_k} + \langle u'_j u'_k \rangle \frac{\partial \langle u_i \rangle}{\partial x_k} \right]$	production rate (PR)
$T_{ij} = - \frac{\partial \langle u'_i u'_j u'_k \rangle}{\partial x_k}$	turbulent diffusion (TD)
$D_{ij} = - \frac{1}{Re_\tau} \frac{\partial^2 \langle u'_i u'_j \rangle}{\partial x_k \partial x_k}$	viscous diffusion (VD)
$\Pi_{ij} = - \left[\frac{\partial \langle p' u'_i \rangle}{\partial x_j} + \frac{\partial \langle p' u'_j \rangle}{\partial x_i} \right]$	pressure–velocity diffusion (PV)
$\pi_{ij} = \left\langle p' \left(\frac{\partial u'_i}{\partial x_j} + \frac{\partial u'_j}{\partial x_i} \right) \right\rangle$	pressure strain correlation (PS)
$\varepsilon_{ij} = - \frac{2}{Re_\tau} \left\langle \frac{\partial u'_i}{\partial x_k} \frac{\partial u'_j}{\partial x_k} \right\rangle$	dissipation rate (DS)
$N_{ij} = - N_\tau \Omega_i (\varepsilon_{ilk} \langle u'_k u'_j \rangle + \varepsilon_{jlk} \langle u'_k u'_i \rangle) / \Omega$	Coriolis force velocity correlation (CO)

The transport equation for the fluctuating enstrophy is

$$\frac{\partial \langle \omega'_i \omega'_i \rangle / 2}{\partial t} + \langle u_k \rangle \frac{\partial \langle \omega'_i \omega'_i \rangle / 2}{\partial x_k} = \text{PR}^{\text{GR}} + \text{PR}^{\text{TV}} + \text{PR}^{\text{MV}} + \text{PR}^{\text{MM}} + \text{PR}^{\text{RM}} + \text{TR} + \text{VD} + \text{DS} \quad (\text{A.2})$$

where the terms on the right-hand side are

$\text{PR}^{\text{GR}} = - \langle \omega'_i u'_k \rangle \frac{\partial \langle \omega_i \rangle}{\partial x_k}$	gradient production by fluctuating velocity
$\text{PR}^{\text{TV}} = \left\langle \omega'_i \omega'_k \frac{\partial u'_i}{\partial x_k} \right\rangle$	production by the fluctuating velocity gradient
$\text{PR}^{\text{MV}} = \langle \omega'_i \omega'_k \rangle \frac{\partial \langle u_i \rangle}{\partial x_k}$	production by the mean velocity gradient
$\text{PR}^{\text{MM}} = \langle \omega_k \rangle \left\langle \omega'_i \frac{\partial u'_i}{\partial x_k} \right\rangle$	mixed production by the mean vorticity
$\text{PR}^{\text{RM}} = N_\tau \Omega_k \left\langle \omega'_i \frac{\partial u'_i}{\partial x_k} \right\rangle / \Omega$	mixed production by the system rotation
$\text{TR} = - \left\langle u'_k \frac{\partial \langle \omega'_i \omega'_i \rangle / 2}{\partial x_k} \right\rangle$	turbulent transport by the fluctuating velocity
$\text{VD} = \frac{1}{Re_\tau} \frac{\partial \langle \omega'_i \omega'_i \rangle / 2}{\partial x_k \partial x_k}$	viscous diffusion
$\text{DS} = - \frac{1}{Re_\tau} \left\langle \frac{\partial \omega'_i}{\partial x_k} \frac{\partial \omega'_i}{\partial x_k} \right\rangle$	dissipation rate

References

- [1] Johnston JP, Halleen RM, Lezius DK. Effects of spanwise rotation on the structure of two-dimensional fully developed turbulent channel flow. *J Fluid Mech* 1972;56:533–57.
- [2] Johnston JP. The suppression of shear layer turbulence in rotating systems. *ASME J Fluids Eng* 1973;95:229–36.
- [3] Bradshaw P. The analogy between streamline curvature and buoyancy in turbulent shear flow. *J Fluid Mech* 1969;36:177–91.
- [4] Tritton DJ, Davies PA. In: Swinney HL, Gollub JP, editors. *Hydrodynamic instabilities and the transition to turbulence*. Springer; 1981. p. 229.
- [5] Tritton DJ. Stabilization and destabilization of turbulent shear flow in a rotating fluid. *J Fluid Mech* 1992;241:503–23.
- [6] Kristoffersen R, Andersson HI. Direction simulation of low-Reynolds-number turbulent flow in a rotating channel. *J Fluid Mech* 1993;256:163–97.
- [7] Koyama HS, Ohuchi M. Effects of Coriolis force on boundary layer development. In: *Proceedings of the 5th symposium on turbulent shear flows*. Ithaca, 1985. p. 21.19–24.
- [8] Watmuff JH, Witt HT, Joubert PN. Developing turbulent boundary layers with system rotation. *J Fluid Mech* 1985;157:405–48.
- [9] Ibal G. Adverse pressure gradient and separating turbulent boundary layer flows with system rotation. Ph.D. Thesis, University of Melbourne, 1990.
- [10] Moin P, Kim J. Numerical investigation of turbulent channel flow. *J Fluid Mech* 1982;118:341–77.
- [11] Orlandi P. Helicity fluctuations and turbulent energy production in rotating and non-rotating pipes. *Phys Fluids* 1997;9:2045–56.
- [12] Rogers MM, Moin P. Helicity fluctuation in incompressible turbulent flows. *Phys Fluids* 1987;30:2662–71.
- [13] Tsinober A, Eggels JGM, Nieuwstadt FTM. On alignments and small scale structure in turbulent pipe flow. *Fluid Dyn Res* 1996;16:297–310.
- [14] Wang MH, Fu S, Zhang GH. Large-scale spiral structures in turbulent convection between two vertical plates. *Phys Rev E* 2002;66:066306.
- [15] Wu JZ, Zhou Y, Lu XY, Fan M. Turbulent force as a diffusive field with vortical sources. *Phys Fluids* 1999;11:627–35.
- [16] Moffatt HK, Tsinober A. Helicity in laminar and turbulent flow. *Annu Rev Fluid Mech* 1992;24:281–312.
- [17] Mansour NN, Kim J, Moin P. Reynolds-stress and dissipation-rate budgets in a turbulent channel flow. *J Fluid Mech* 1988;194:15–44.
- [18] Kim J, Moin P, Moser R. Turbulence statistics in fully developed channel flow at low Reynolds number. *J Fluid Mech* 1987;177:133–66.
- [19] Durbin PA. Near-wall turbulence closure modeling without “damping functions”. *Theo Comp Fluid Dyn* 1991;3:1–13.
- [20] Orlandi P, Ebstein D. Turbulent budgets in rotating pipes by DNS. *Int Heat Fluid Flow* 2000;21:499–505.
- [21] Tennekes H, Lumley L. *A first course in turbulence*. Cambridge (MA): MIT; 1972.
- [22] Leighton RI, Swann Jr TF, Handler RA, Swearingen JD. Interaction of vorticity with a free surface in turbulent open channel flow. In: *AIAA 29th aerospace science meeting*, Reno, Nevada 1991, AIAA Paper No. 91-0236.
- [23] Antonia RA, Kim J. Low-Reynolds-number effects on near-wall turbulence. *J Fluid Mech* 1994;276:61–80.
- [24] Lamballais E, Lesieur M, Métais O. Effects of spanwise rotation on the vorticity stretching in transitional and turbulent channel flow. *Int J Heat Fluid Flow* 1996;17:324–32.
- [25] Dimitropoulos CD, Sureshkumar R, Beris AN, Handler RA. Budgets of Reynolds stress, kinetic energy and streamwise enstrophy in viscoelastic turbulent channel flow. *Phys Fluids* 2001;13:1016–27.
- [26] Verzicco R, Orlandi P. A finite difference scheme for direction simulation in cylindrical coordinates. *J Comput Phys* 1996;123:402–14.

- [27] Kim J, Moin P. Application of a fractional-step method to incompressible Navier–Stokes equations. *J Comput Phys* 1985;59:308–23.
- [28] Rai MM, Moin P. Direct simulations of turbulent flow using finite-difference schemes. *J Comput Phys* 1991;96:15–53.
- [29] Orlandi P, Fatica M. Direct simulations of turbulent flow in a pipe rotating about its axis. *J Fluid Mech* 1997;343:43–72.
- [30] Pan YK, Tanaka T, Tsuji Y. Direct numerical simulation of particle-laden rotating turbulent channel flow. *Phys Fluids* 2001;13(8):2320–37.
- [31] Chung SY, Rhee GH, Sung HJ. Direct numerical simulation of turbulent concentric annular pipe flow Part 1: flow field. *Int J Heat Fluid flow* 2002;23:426–40.
- [32] Vittor G, Verzicco R. Direct simulation of transition in an oscillatory boundary layer. *J Fluid Mech* 1998;371:207–32.
- [33] Quadrio M, Sibilla S. Numerical simulation of turbulent flow in a pipe oscillating around its axis. *J Fluid Mech* 2000;424:217–41.
- [34] Grossmann S, Lohse D. On geometry effects in Rayleigh–Bénard convection. *J Fluid Mech* 2003;486:105–14.
- [35] Dong YH, Lu XY. Direct numerical simulation of stably and unstably stratified turbulent open channel flows. *Acta Mech* 2005;177: 115–36.
- [36] Li BY, Liu NS, Lu XY. Direct numerical simulation of wall-normal rotating turbulent channel flow with heat transfer. *Int J Heat Mass Transfer*, in press.
- [37] Zou LY, Liu NS, Lu XY. An investigation of pulsating turbulent open channel flow by large eddy simulation. *Comput Fluids* 2006;35:74–102.
- [38] Wang L, Dong YH, Lu XY. An investigation of turbulent open channel flow with heat transfer by large eddy simulation. *Comput Fluids* 2005;34:23–47.
- [39] Wang L, Lu XY. Large eddy simulation of stably stratified turbulent open channel flows with low- to high-Prandtl number. *Int J Heat Mass Transfer* 2005;48:1883–97.
- [40] Liu NS, Lu XY. Large eddy simulation of turbulent flows in a rotating concentric annular channel. *Int J Heat Fluid Flow* 2005;26:378–92.
- [41] Liu NS, Lu XY. Large eddy simulation of turbulent concentric annular channel flows. *Int J Numer Meth Fluids* 2004;45:1317–38.
- [42] Dong YH, Lu XY. Large eddy simulation of a thermally stratified turbulent channel flow with temperature oscillation on the wall. *Int J Heat Mass Transfer* 2004;47:2109–22.
- [43] Wang L, Lu XY. An investigation of turbulent oscillatory heat transfer in channel flows by large eddy simulation. *Int J Heat Mass Transfer* 2004;47:2161–72.
- [44] Orlandi P. *Fluid flow phenomena*. Kluwer Academic Publishers; 2000.